Air Force Office of Scientific Research/ Missile Defense Agency Pilot program for Science and Technology Research at HBCU/Minority Institutions

Prediction of Chemical Laser Flow

Peter Vorobieff and C. Randall Truman

April 14, 2006

20060601072

Executive summary

The scope of the work as proposed to the funding agency was to carry out numerical calculations of high-speed mixing flows using GASP, a computational fluid dynamics (CFD) code. The ultimate goal is to use GASP for prediction and optimization of chemical laser flows. To do it, one must have confidence in the performance of the hydrodynamic and mixing part of the code.

For complex numerical simulations, it is essential to perform *code validation* – a quantitative comparison of numerical results with experimental results confirming that the code faithfully reproduces the physics of the real problem. Two detailed validation exercises were performed with GASP:

- **Simulation of a shock-accelerated mixing flow.** This validation exercise compared the numerical results produced by GASP with highly-resolved experimental data on flows subject to Richtmyer-Meshkov instability (RMI), the preferred test problem for quantitative assessment of the performance of CFD codes in prediction of the properties of high-speed mixing flows.
  The validation problem revealed that GASP can faithfully reproduce all the large-scale quantitative properties of the flow. We also gained important additional insights into the strengths and limitations of GASP (and other numerical codes) in prediction of disordered small scales in flows transitioning to turbulence.

- **General jet-in-crossflow problem.** The problem of a supersonic jet discharging into a supersonic crossflow presents a significant computational challenge, yet provides a valuable validation exercise when the results are compared with experimental data.
  The conditions for this exercise were chosen to achieve two goals:

  - Provide comparison with best experimental data available in open literature.
  - Test the code in a generic configuration that can be easily modified to represent a specific chemical laser nozzle injection scheme.

  The agreement with the experimental data was quite good, yet subtle features of the flow that were not apparent in the experiment were revealed by the simulation.

The results of our work are as follows.

- We found the hydrodynamic model used in GASP to be suitable for prediction of mixing in chemical laser flows.

- We found the error in prediction of the geometry of large-scale features (*e.g.*, counter-rotating vortex pairs) not to exceed 10-15% when compared with experiment.

- We found that a fully three-dimensional model is advantageous when the goal is to correctly assess mixing.

- We determined the grid parameters and the appropriate conditions to run the simulation to produce credible results in the range of flow regimes consistent with the operation of a chemical oxygen-iodine laser (COIL). GASP has been validated by comparison with experimental data.

The detailed report that follows begins with an overview of the two validation problems we considered, followed by the description of the computational set-up and the discussion of the results. The work summarized here has been presented at AIAA [1] and APS [2, 3] conferences, as well as in a journal paper currently under review [4].

1 Overview of validation problems

The two validation problems were selected to provide good quantitative comparison with experiment. There are relatively few available data sets characterizing high-speed mixing flow with any level of quantitative detail. Our first validation problem, shock acceleration of a heavy gas cylinder immersed in lighter gas, was chosen because of relatively simple initial conditions, which are nominally two dimensional, making it possible to run a two-dimensional simulation and compare the flow features. The second problem is much more complex geometrically, and it features flow conditions that, while being sufficiently generic, are very close to those in a chemical laser – supersonic injection of gas into a supersonic flow.

In a chemical laser, hydrodynamic mixing of fuel and oxidizer is essential to obtain a population inversion of the excited state at an optimum rate. If mixing is poor, then the chemical reactions occur too slowly, producing few excited atoms in the lasing cavity. On the other hand, if the mixing is too fast then most of the excited atoms will deactivate before reaching the lasing cavity. In Chemical Oxygen Iodine lasers (COIL), the primary flow of singlet delta oxygen (with helium carrier) is passed through a supersonic nozzle to the laser cavity. The fuel (iodine with helium carrier) is injected transversely into the primary flow upstream of the throat in subsonic COIL lasers or downstream of the throat in supersonic COIL lasers. The primary advantage of supersonic COIL is that fuel injection is decoupled from the upstream singlet oxygen generator (SOG). Moreover, fuel and carrier injected upstream of the throat in subsonic COIL must pass through the nozzle throat. Since the fuel is injected downstream of the throat in supersonic COIL, flow velocity increases and the partial pressure of singlet delta oxygen is reduced, both of which reduce the rate of oxygen loss. Several designs for supersonic COIL lasers have been described in the open literature [5, 6, 7, 8, 9, 10, 11]. In all cases, mixing of the fuel with carrier into the primary flow is crucial to chemical laser design. This mixing is achieved by injecting one of the reacting species into the main flow. In turn, this problem is a special case of a more general problem of a jet in crossflow. The latter has been the subject of some detailed experimental studies that provide sufficient data for experimental validation presented in the following sections of this report.

1.1 Shock acceleration of a gas cylinder

Richtmyer-Meshkov instability (RMI) occurs when an incident shock accelerates an interface between two fluids of different densities and thus amplifies any initial perturbation present on the interface. This interfacial instability was theoretically predicted in 1960 by a Los Alamos theorist, R.D. Richtmyer [12], and first experimentally observed in 1969 by a Russian experimentalist, E.E. Meshkov [13]. It is of importance to applications ranging from astrophysics [14], inertial confinement fusion [15] to supersonic combustion [16, 17]. The fluid configuration leading to a frequently considered RMI problem is shown in Fig. 1. Two fluids with different properties are separated by an initially diffuse interface. The shock travels from light fluid (gray color) to heavy fluid (black color) through the interface. The development of RMI for this configuration can be divided into three stages. The short initial stage is *linear*. In this stage, the incident shock wave collides with a perturbed material interface and bifurcates into a transmitted shock and a reflected wave. In Fig. 1, left, the pressure and density gradients are locally misaligned. This misalignment leads to baroclinic generation of vorticity at the interface. The resulting vortex roll-up (Fig. 1, right) leads to growth of the perturbation amplitude of the interface. The perturbation amplitude is very small as compared to the wavelength of the interface and hence the growth of interface can be safely assumed to be linear [12, 18]. Compressibility effects are important in this stage [12]. The flow-field in this stage is deterministic. Later in this stage, spikes and bubbles appear on the interface. A bubble is a portion of the light fluid penetrating into the heavy fluid and a spike is a portion of the heavy fluid penetrating into the light fluid.

The second stage is *nonlinear deterministic*. In this stage the spikes and bubbles grow substantially. The amplitude of perturbation grows to the order of the wavelength and hence now the flow is nonlinear. In the later part of this stage, roll-up of material into the vortex cores occurs. Roughly at the same time, small scales also appear in the flow. The small scale appearing on the outer edge of the large scale vortex core may be due to shear-induced secondary instability while the small scale appearing on the inner edge may be due to secondary baroclinic instability [19, 20, 21]. In this stage, the large scales in the flow are deterministic [22, 23] while the small scales are stochastic. Rightley *et al.* [24] refer to this stage as to *ordered turbulence*. In general, CFD codes can reliably predict the large scales but not the small scales [25].

The third stage is *disordered turbulence* [25]. In this stage, the secondary instabilities become pronounced and lead to the onset of turbulence with chaotic mixing. Being turbulent in nature, this stage is dominated by three-dimensional physics, unlike the first two stages.

The development of RMI depends heavily on the initial conditions that influence the vorticity deposition in the early stages of RMI evolution, and small changes in the initial conditions can lead to profound changes in the late-time flow morphology, as discussed by Budzinski and Benjamin [26]. RMI has several practical applications of importance (some of which were mentioned above), including strong explosions and inertial confinement fusion, which makes reliable numerical simulation of RMI-driven flows a priority. At the same time, the limited energy input into the RMI-driven flow, the gradual evolution of the initially deterministic flow towards disorder and the dependence on the initial conditions makes RMI an attractive problem for a more general study of transition to turbulence. Advances in experimental diagnostics in the recent years have produced highly resolved quantitative benchmarks that can be used to validate numerical codes. We performed a detailed comparison of a 2D (two-dimensional) numerical simulation of an RMI-driven flow with a nominally 2D initial condition geometry commonly used for code validation with experimental results. The large-scale flow structure observed in experiment is faithfully reproduced by the numerics. The numerical results also show the emergence of a secondary instability which has been observed in experiment. However, the statistics of the small-scale features due to this secondary instability are quite different for the simulation and the experiment. This difference is likely due to the fact that the scalings for the disordered features are dictated by the dimensionality of the flow. This imposes limitations on the applicability of 2D simulations to flows with inherently 3D (three-dimensional) small-scale structure evolving, even if the initial conditions and the large-scale structure of the realizations of such flows are effectively 2D.

For RMI the fluid configuration must have an initially perturbed (non-planar) density interface subjected to impulsive acceleration. A geometrically simple interface (Fig. 1) can be realized experimentally by injecting a cylinder of sulfur hexafluoride SF_6 into lighter air. The interface between the air and the heavier SF_6 is diffusive. The flow is impulsively accelerated by a planar shock. This problem has been the subject of several experimental studies [27, 28, 29], producing flow visualization and qualitative data. These are the experimental results we compare with the results of our numerical simulation.

1.2 Supersonic jet in crossflow (JICF)

Sonic injection into a crossflow (whether subsonic or supersonic) that occurs in chemical lasers is a special case of the more general problem of a Jet in Crossflow (JICF)), the subject of the current work. Mixing is expected to be dominated by vortical structures and shock structures produced by this interaction. In particular, the counter-rotating vortex pair (CRVP) formed in the jet-freestream interaction dominates downstream mixing. Earlier research on JICF was focused on the understanding of mixing [30, 31, 32, 33, 34, 35]. Moreover, reliable experimental data for JICF cases is available for comparison with numerical simulations of a flow similar to that which occurs in a chemical laser nozzle. Of specific interest to us is the work of Gruber *et al.* [35] who performed an experimental mixing study of a sonic jet injected into supersonic crossflow at Mach 1.98 revealing the overall structure of the flow. The main flow was comprised of air, with injection either of air or of helium into the flow. The dominant flow structures observed in a typical JICF configuration involving a sonic jet and supersonic crossflow are shown in Figure 2. The adverse pressure gradient causes the turbulent boundary layer to separate and form recirculating zones upstream and downstream of injection. The jet obstructs the supersonic crossflow and thus leads to the formation of a three-dimensional bow shock. The underexpanded sonic jet undergoes expansion forming Prandtl-Meyer expansion fans and a system of incident-reflected oblique shocks. The barrel shock is the barrel-shaped structure formed due to the expansion fan which terminates in the Mach disk. The horseshoe vortex and wake vortices are formed downstream of the injection. The counter rotating pair of vortices (CRVP) dominates the cross-section of the jet in the far field and improves mixing by entraining the crossflow fluid. The dominant structure that apprently governs the mixing in both validation problems,

despite many differences in the conditions, is a counter-rotating vortex pair.

2 Numerical code

GASP, an acronym for General Aerodynamic Simulation Program, is a CFD code from AeroSoft Inc., Blacksburg, VA. GASP is a structured multi-block CFD solver that solves an integral form of the Reynolds Averaged Navier Stokes (RANS) equations as well as simplified RANS equations such as thin-layer RANS, parabolized RANS, Euler equations and incompressible RANS. Density and pressure are time-averaged (Reynolds-averaged) while temperature and velocity components are mass-weighted averages (or Favre averages). For compressible or reacting flows Favre averaging is favorable since it incorporates the density changes while averaging the Navier-Stokes equations. GASP uses a cell-centered finite volume method. GASP has a variety of user-selectable features to deal with compressible, mixing, and reacting flows, and it incorporates several turbulence models [37].

A wide variety of flows has been studied using GASP including flows in a combustion chamber and flows over reentry vehicles. GASP code includes support for COIL (chemical oxygen iodine laser) capability developed with support from AFRL and AFOSR. GASP is being used by NASA for verification purposes [38]. The following section describes the numerical formulation of our problems with GASP.

3 Numerical Formulation

Our simulations involve two species (air and SF_6 for the first problem, air and helium for the second), and the flow is considered to be compressible and non-reacting. As mentioned above, we use a commercial CFD solver GASP that solves the Navier-Stokes equations with a cell-centered finite volume method. The fluxes at the cell faces are found using the MUSCL (Monotonic Upstream-centered Scheme for Conservation Laws) scheme. Several flux splitting methods can be implemented in GASP, with the possibility to assign a different inviscid flux scheme in each direction (x, y, z). The motivation for flux splitting is provided by the necessity to model flows with local subsonic and local supersonic areas. In the former, flow information travels both upstream and downstream, while in the latter it is downstream only, which can pose considerable problems unless flux splitting is implemented. In our case, the interpolation of primitive variables (from cell center to cell faces) is third-order upwind biased [37]. In the case of the first validation problem, the flux scheme involves an assumption of no flux in the direction normal to the plane of the flow to enforce two-dimensionality. In the plane of the flow, Roe's upwind inviscid flux scheme [39] is used for the first validation problem. Based on inviscid 2D simulations, the Roe with Harten flux scheme was chosen for the second problem.

The viscous terms are discretized using a central differencing scheme and have nominally second-order spatial accuracy. The laminar transport properties (viscosity and thermal conductivity) are specified for each species. For diffusivity, Fick's law of binary diffusion is used, which takes into account only the effect of concentration gradient. The laminar properties are calculated for each species in the flow. Then the laminar properties for the mixture are assessed using Wilkes' mixing model. Species are assumed to have different densities, but pressure, velocity components and temperature are based on the mixture and not the individual species (*partial multi-fluid formulation*). The binary mixture is assumed to have a single adiabatic exponent.

GASP uses either an explicit Runge Kutta algorithm or an implicit dual time stepping algorithm. The implicit dual time stepping algorithm has two steps. In the first step, the time dependent source term is added to the residual. During the second step, the physical time is kept constant while the residual is driven to zero. GASP uses MPI for parallelization. The computational grid is imported into GASP in plot3d format. The load balancing on different processors can be either manual or automatic. We employed the dual time-stepping algorithm with automatic load balancing.

GASP allows the use of several turbulence models, from algebraic to $k - \epsilon$, $k - \omega$ and a Reynolds stress model. In the case of a shock-accelerated flow (validation problem 1), the flow is initially at rest, and the shock interaction leads to formation of a large-scale vortex structure which *eventually* transitions to turbulence, however, small scales take time to develop. Moreover, from experiment we have *a priori* knowledge [19, 27] regarding the emergence of small-scale flow features in our transitional flow, and in the time interval of interest, these features should be resolvable with the fine mesh described later in this report. The dimensionality of the small scales is also discussed later. Thus no turbulence model was used for validation problem 1. Viti *et al.* [40] found that for a problem similar to our second JICF validation problem the 1998 $k - \omega$ turbulence model was an optimum choice considering accuracy and computational

time. Thus we selected $k - \omega$ for the JICF calculations. The wall in the JICF setup was assumed smooth by setting the dimensionless roughness to $K_r^+ = 1$.

The Navier-Stokes equations describing the flow under these assumptions can be represented, using the standard *Einstein notation*, as shown below.

Mass conservation and molecular diffusion :

$$\frac{\partial \rho_n}{\partial t} + \frac{\partial \rho_n u_i}{\partial x_i} = -\frac{\partial \rho_n \tilde{v}_{ni}}{\partial x_i} \tag{1}$$

where $\tilde{v}_{ni}$ is mass diffusion velocity of the species n in i direction. Now from Fick's law of binary diffusion :

$$\rho_n \tilde{v}_{ni} = -\rho_m D_{nm} \frac{\partial c_n}{\partial x_i}$$

where c_n represents concentration of species n and D_{nm} is the diffusion coefficient of species n with respect to species m. In GASP this diffusion coefficient can be calculated using laminar viscosity (μ_l) and laminar Schmidt number (Sc_l) as :

$$D_{nm} = \left(\frac{\mu_l}{\rho Sc_l}\right)_{nm}$$

We used a constant $Sc_l = 0.7$ for the first problem (air and sulfur hexafluoride). For the second problem, the laminar Schmidt number for air injection was 0.7 (resulting in negligible molecular diffusion), while for helium injection it was 0.3. The turbulent Schmidt number was 0.5 for all cases. The simulation was performed assuming steady-state conditions. The pseudo-time steps for the second problem were based on specifed CFL number (local at first and then global).

Momentum conservation :

$$\frac{\partial \rho u_i}{\partial t} + \frac{\partial}{\partial x_i}\left(\rho u_i u_i + p \delta_{ij}\right) = \frac{\partial \tau_{ij}}{\partial x_i} \tag{2}$$

where δ_{ij} is the standard Kronecker delta such that :

$$\delta_{ij} = 0 \text{ when } i \neq j \text{ and}$$

$$\delta_{ij} = 1 \text{ when } i = j$$

and τ_{ij}, the shear-stress, given by (for Newtonian fluid) :

$$\tau_{ij} = \mu_l \left(\frac{\partial u_i}{\partial x_j} + \frac{\partial u_j}{\partial x_i}\right) - \frac{2}{3}\mu_l \frac{\partial u_k}{\partial x_k}\delta_{ij}$$

Energy Conservation :

$$\frac{\partial \rho e_0}{\partial t} + \frac{\partial}{\partial x_i}\left(\rho e_0 u_i + p u_i + \rho e_0 u_i\right) = \frac{\partial}{\partial x_i}\left(\tau_{ij} u_j\right) - \frac{\partial q_i}{\partial x_i} \tag{3}$$

where

$$e_0 = e + \frac{u_i u_i}{2}$$

$$q_i = -k\frac{\partial T}{\partial x_i}$$

On the time scale of interest, the contribution of heat conduction is not significant. Thus the heat transfer coefficient k was set at a constant value corresponding to that of air.

Now, since we have two species (n, m : 1, 2) and two or three coordinates (i, j : 1, 2 or 1, 2, 3), the equations (1), (2) and (3) can be finally closed by assuming each of the species to be thermally and calorically perfect and using the thermal equation of state :

$$p = \rho R T \tag{4}$$

along with the thermodynamic relation :

$$e = C_v T \tag{5}$$

5

By using the Gauss theorem, the above system of equations can be easily represented in the standard integral form, which then is numerically solved in GASP. The code is nominally second-order in time and third-order upwind-biased in space. To prevent numerical oscillations near the shock front, we used a Min-Mod limiter [37, 41]. The limiter reduces the spatial accuracy to first-order in the vicinity of the shock and hence in general the observed spatial accuracy may be lower than the nominal spatial accuracy.

4 Numerical Simulation

Details specific to the simulation of each of the problems we considered are presented below. In both cases, we made an effort to minimize the computational resources required for the simulation.

4.1 Shock accelerated gas cylinder

The computational domain is shown in Fig. 3. The domain along the y-direction was reduced to 1.0 cm from the physical 3.75 cm half-width of the shock tube by applying second-order extrapolation at y = 1.0 cm. The domain along the x-direction was reduced significantly as opposed to the physical length of the shock tube. This is achieved by using the upstream condition of the shock in the test section. The variation of pressure in the shock tube is shown in Fig. 4.

The pressure behind the shock drops from p_0 to p_1 and hence when the shock hits the SF$_6$ cylinder in the test section, it has upstream conditions corresponding to pressure p_1. These upstream conditions are specified as the initial conditions for the shocked region (the shaded region in Fig. 3) and an inflow boundary condition is used at $x = 0$ cm. When the shock hits the SF$_6$ cylinder, it bifurcates into a reflected shock wave and a transmitted shock wave. The reflected shock does not affect the development of RMI. To achieve this numerically, we change the boundary condition at $x = 0$ to reflective, at the time when the front of the reflected shock wave reaches $x = 0$ cm. The evolving SF$_6$ cylinder has finite velocity and to ensure that it stays within the computational domain, a uniform negative velocity is superimposed on the flow in the x-direction. It is important to note that the SF$_6$ cylinder must not travel towards the $x = 0$ boundary because that would lead to interaction between the reflected shock and SF$_6$ cylinder.

The values for time step (Δt) and grid spacing (Δx) were found in a convergence study. In RMI, the moving shock has the highest propagating speed and this specifies the limiting values for Δt and Δx. Hence a one-dimensional moving shock problem was simulated to determine Δt and Δx. Grid sizes of 100 μm, 200 μm and 800 μm were used. After obtaining convergence at $\Delta x = 200$ μm, different time steps (Δt) were used. The solution converged for $\Delta t = 0.125$ μs. After the shock passed through the computational domain, the value for Δt was increased by a factor of 6.

Table 1: Shock tube conditions

Property	Upstream of shock	Downstream of shock
Pressure (Pa)	121100	80000
x-velocity (m/s)	104.9	0
y-velocity (m/s)	0	0

Second-order accuracy in time and third-order accuracy in space were used to predict RMI-driven flow evolution. As it was mentioned earlier, the effective accuracy of the code is lowered by the use of limiters in the immediate vicinity of the shock. However, this should have a relatively small effect on the evolution of the flow after the shock passage. For the viscous case, the Sutherland viscosity model was used for each species, and the mixture kinematic viscosity was obtained from Wilkes' law. An implicit dual time stepping Gauss-Seidel scheme was employed as the temporal algorithm. The initial conditions are shown in Table 1. The initial distribution of SF$_6$ is based on a simple Gaussian fit to the experimental data [42, 43], with the peak volume fraction of SF$_6$ at 80%.

Table 2: JICF conditions

Quantity	Case: Air	Case: Helium
Crossflow Gas	Air	Air
Injectant Gas	Air	Helium
p_∞ (kPa)	41.8	41.8
T_∞ (K)	169	168
u_∞ (m/s)	516	515
M_∞	1.98	1.98
ρ_∞ (kg/m^3)	0.860	0.866
μ_∞ (Pa-s)	$1.15\,x10^{-5}$	$1.14\,x10^{-5}$
$Re_\infty = (\rho_\infty.U_\infty)/\mu_\infty$ (m^{-1})	$3.87\,x10^7$	$3.91\,x10^7$
p_j (kPa)	476	405
T_j (K)	250	225
u_j (m/s)	317	882
M_j	1	1
ρ_j (kg/m^3)	6.64	0.867
μ_j (Pa-s)	$1.60\,x10^{-5}$	$1.62\,x10^{-5}$
$Re_j = (\rho_{e,j}.U_{e,j}.D_j)/\mu_{e,j}$	$8.36\,x10^5$	$3.00\,x10^5$
γ_j	1.4	1.67
$J = \frac{\rho_j u_j^2}{\rho_\infty u_\infty^2}$	2.90	2.90

4.2 Jet in cross-flow

The conditions for our simulations were selected to coincide with those in the experiments of Gruber *et al.* [35], as summarized in Table 2 listing the static values of pressure, temperature, *etc.* for the two cases we considered (air and helium injection).

The computational domain is shown in Fig. 5. The diameter of the circular injector is $D = 6.35$ mm. The injector was simulated as a constant area duct extending from $-2 <= \frac{y}{D} <= 0$. The structured grid was generated using *Gridgen*, commercial meshing software capable of generating 3D structured and unstructured grids [44]. For the grid convergence study, we used $D = 6$ mm and the downstream domain extended to $\frac{x}{D} = 10$. Our fine grid had $4.7x10^6$ grid points. Using the GASP capability of removing *every other* grid point, the medium grid ($6.1x10^5$ grid points) and coarse grid ($8.1x10^4$ grid points) were generated by two successive coarsenings of the fine grid. The grid had about 8 partially independent (in one direction) zones, with the total number of zones being 34. Pressure and temperature were monitored at the wall of the duct ($y = 0, z = 0$) to determine convergence with respect to the number of cycles.

A *no-slip adiabatic (split)* boundary condition was imposed at the wall ($\frac{y}{D} <= 0$), except over the injection hole. Turbulent boundary layer profiles of primitive variables were specified as crossflow inflow conditions (at $\frac{x}{D} = -8$). These boundary layer profiles were generated using the space-marching capability of GASP and were verified with boundary layer code EDDYBL [45]. To match the experiments, we ensured that the boundary layer thickness approaching the injector was about 1D. Freestream conditions for the boundary layer were the same as those listed in Table 2. Inlet conditions for the injector flow at $\frac{y}{D} = -2$ were uniform stagnation pressure and temperature across the duct, specified to produce Mach 1 flow at the injection hole $\frac{y}{D} = 0$ and to match the experimental static pressure and temperature. The *no-slip adiabatic (split)* boundary condition was applied at the wall of the injector duct. For other outflow boundary conditions, we used first-order extrapolation.

The experiments performed by Gruber *et al.*[35] and Fric and Roshko [46] show that the JICF flow field is highly unsteady and asymmetric. In particular while simulating JICF, Madden and Miller [47] found that the assumption of symmetry and steadiness affects the development of wake vortices and shear layer vortices. However, transient calculations on the full computational domain requires prohibitive computational time for this study. Thus we assumed symmetry and steadiness for our simulation.

7

5 Results

The results from simulations are qualitatively and quantitatively compared with the experiments as described below for each problem.

5.1 Shock-accelerated gas cylinder

The experimental single-cylinder data from the LANL DX-3 shock tube described earlier were published in several papers by Vorobieff et al.[27], and Tomkins et al. [28, 29]. Here we mostly use the work of Tomkins et al. [29] for validation. Numerical simulation may not predict the physics accurately due to its discrete nature. Also the 2-dimensional assumption may not be valid at late times when secondary instabilities become important. Hence we have also done a comparison with the 2-dimensional simulations done by Greenough et al. [42].

The widths and heights of the mixing zone produced by shock acceleration of the SF_6 cylinder (Fig. 6a) and the spacing between the vortex cores of large scale counter-rotating vortices (Fig. 6b) are used for quantitative comparison between experiment and simulation. Mesh refinement described in section 4.1 does not exert much influence on the dimensions of the large-scale vortices, which supports the use of the one-dimensional model discussed earlier to determine mesh spacing. However, the predictions of small-scale secondary instabilities are strongly influenced by mesh spacing (Fig. 7). Note that the secondary instabilities are not symmetric and hence the full computational domain must be used unlike the one shown in Fig. 3. Decreasing the mesh spacing (Δx) also implies decreasing the time step (Δt) so as to keep the ratio $\Delta x / \Delta t$ constant. Hence when the mesh spacing is halved, the computational time increases by a factor of 8. The computations were performed on a Linux cluster consisting of 128 parallel processors (256 MB RAM per CPU). The computational time for varying mesh spacings is shown in Table 3. Considering all these factors, we decided to keep the final mesh spacing as 50 μm. Henceforth, numerical simulations imply a full computational domain with 50 μm as the mesh spacing.

Table 3: Computational Time for validation problem 1.

Mesh Size (μm)	Computational Time
200	1.36 hours
100	10.9 hours
50	3.6 days
25	29 days
12.5	232 days

The qualitative comparison of flow fields acquired in experiments and by our numerical simulation is shown in Fig. 8. The evolution of the vortex pair, including spikes and bubbles, is evident in our simulations. A notch at the axis of symmetry of the cylinder appears in the simulations at earlier times, as can be seen in the experiments as well. This is likely due to shock wave focusing. The cylinder appears to evolve somewhat slower in the simulations and the small-scale structures appear at later times than observed in experiments. This could indicate a problem with vorticity deposition during the initial stage of the RMI simulation. For a future study elucidating the issue, it would be highly desirable to procure early-time experimental velocity fields.

The secondary shear induced instability and baroclinic instability, as explained earlier, are visible in our results. The secondary instabilities in our simulations compare well with these from the simulations of Greenough et al.[42] and Rider et al. [43] using the Raptor code at 800 μsec with comparable mesh sizes. Raptor, as described by Howell and Greenough [48], is a multi-physics adaptive-mesh refinement (AMR) code that uses a second-order (both in space and time) Godunov method to solve Euler equations.

The height and width of the mixing zone (defined as the horizontal and vertical extent of the perturbed SF_6 cylinder), and the vortex spacing are used for quantitative comparison between experiment, our simulation and the simulation done by Greenough et al. [42]. Vortex spacing from experiments was not available for early times and was not provided by Greenough et al. [42]. These comparisons are shown in Fig. 9. The results show that the overall trend of our simulation is consistent with the experiments as well as with the simulations done by Grenough et al. [42]. There is some difference in early-time predictions between our simulations and those produced by the Eulerian

AMR codes, with the latter actually reproducing the early-time evolution of the mixing zone width better (Fig. 9, top). This difference could be due to the limiter used in our code to avoid fluctuations near the shock front. At later times, however, the differences between our results and the experiments are very close to those between predictions of Greenough et al.[42] and experiments. This illustrates the often-overlooked point that quantitative agreement between two simulations does not necessarily mean that the same degree of agreement exists between either of the simulations and the experiment.

The work described above used an axisymmetric Gaussian density distribution for the initial conditions. However, in experiments the initial conditions are always subjected to small perturbations, often resulting in appreciable deviations from radial symmetry (about 10 percent in terms of the concentration field, according to Dwarkadas et al. [49]). To simulate the effect of such perturbations on the evolution of the flow, we introduced small deviations into the initial conditions as follows. The circular distribution was replaced with a slightly elliptical one, with the ratio between the major axis and the minor axis 1.05. The angle θ between the major axis of the ellipse and the direction of the shock was varied in increments of 22.5° between 0° and 90°, resulting in five sets of initial conditions.

Figure 10 shows the evolution of the flow developing from these initial conditions in our simulation. At early times, variation of the initial conditions has little influence on the apparent flow structure. The only flow feature directly affected is the spike produced by shock focusing (Fig. 10, top row closeups). Loss of symmetry along the centerline in the direction of the shock propagation leads to the distortion of the spike very similar to that observed in most experiments.

At late times, the overall flow morphology remains the same, manifesting the large-scale structure produced by the initial RMI-induced vorticity deposition and the smaller structures emerging due to the secondary instabilities. The specific features of these small-scale structures (e.g., position) vary for different θ, in a fashion similar to that observed in experiment for initial conditions with small perturbations inherently present. Thus it can be concluded that in the "viewgraph norm" the simulation agrees with the experiment. Moreover, the simulation captures an important feature of the RMI-driven cylinder flow in the stage of incipient turbulence: while the large-scale structure is reliably reproducible from experiment to experiment, the small scales are disordered. In the simulation, this disordering is produced by a subtle change in the initial conditions.

In the analysis of experimental measurements, both the density fields [29] and the velocity fields [27] have been ensemble-averaged. One could expect quantitative agreement between these ensemble-averaged results and similar results from a RANS code. By subtracting the ensemble average from the instantaneous experimental fields, fluctuation fields were produced as well. Statistical analysis of the instantaneous, ensemble-average and fluctuation velocity fields [27] acquired in experiments as the flow transitions to turbulence revealed some interesting trends. The statistics of the flow were analyzed in terms of the longitudinal velocity structure functions

$$S_n(r) = \left\langle \left[(\mathbf{u}(\mathbf{x} + \mathbf{r}) - \mathbf{u}(\mathbf{x})) \cdot \frac{\mathbf{r}}{|\mathbf{r}|} \right]^n \right\rangle,$$

where $\mathbf{u}$ is the velocity vector, $r = |\mathbf{r}|$ and $< \ldots >$ denotes ensemble-averaging. For the second-order velocity structure function $S_2(r)$, it was found that the late-time ($\sim$ 1300 μs) behavior of the instantaneous field structure function approaches the 2/3 power law, consistent with Kolmogorov's 1941 theory of fully developed turbulence. This result was not altogether surprising, as the flow is transitioning to turbulence. What was more interesting was the emergence of the similar behavior at a much earlier time ($\sim$ 760 μs) in the structure functions of the *fluctuating* velocity. These observations were based on the measurements of two velocity components in a plane normal to the axis of the cylinder, with an effective grid resolution of about 70 μm. The question that arises quite naturally is whether the same trends can be observed in the analysis of our numerical data.

Figure 11 shows the structure functions $S_2(r)$ produced by ensemble-averaging of the velocity fields at $\sim$ 900 μs developing from the five sets of elliptic initial conditions described above. It is noteworthy that the overall agreement of the instantaneous and ensemble-averaged structure function behavior with experiment is fairly good. Also like in the experiment, the behavior of the fluctuating velocity structure function is distinctly different. Here, however, is where the similarity between experiment and theory ends. While the fluctuating velocity field structure function in experiment shows a trend towards 2/3 power-law scaling starting as early as $\sim$ 760 μs, the fluctuating components of the numerical data exhibit a distinctly different behavior, with the fluctuation structure function S_2 growth with r falling far short of the 2/3 power law. Is this surprising? Perhaps it should not be, as the fluctuating features in experiments are three-dimensional, while similar features in numerics are confined to two dimensions, and no simple increase in grid resolution is likely to eliminate this problem, even if the 2D grid resolves the Kolmogorov scale. In the latter case, analysis of fluctuations in the flow developing from small changes in the initial conditions is likely to

reveal statistics consistent with those predicted and experimentally observed for spatially two-dimensional turbulence (see, for example, Vorobieff *et al.* [50]). The latter leads to scalings distinctly different from those predicted by the Kolmogorov theory and observed in 3D experiments. Thus the comparison of the fluctuating component scalings in experiments and numerics reveals an important physics issue of limitations inherently present in a 2D simulation of a spatially 3D unstable flow.

In simulations performed for an inviscid case, there was no appreciable difference observed in the results. This supports the notion that viscous dissipation is of relatively small importance on the time scale considered here ($<$ 1000 μs), and the exact choice of laminar properties does not have much influence on the flow. We also performed the simulations for 60% peak SF_6 concentration. In this case, the SF_6 cylinder seems to evolve at a faster rate and the secondary instabilities were observed at times much earlier than the 80% case. This can be attributed to steeper gradients in the Gaussian distribution for the 60% case (so that the total concentration of SF_6 is the same in both cases) as compared with the 80% case. Steeper gradients in density fields imply stronger baroclinic deposition and hence faster evolution of the SF_6 cylinder. For space constraints, the results are not presented here. The peak concentration of SF_6 in the initial conditions in the experiments is subject to some fluctuations, and an accurate measurement of the initial concentration field, as well as the early-time velocity field, as mentioned earlier, should help resolve the discrepancy. Zhang *et al.* [21] recently adopted a feedback approach to resolve the uncertainty in experiments. They have used a finite thickness layer located between SF_6 and air. The parameters of this finite layer are changed with iterations until good agreement is achieved between the simulations and experiments [20, 21]. Zoldi [36] also concluded such need to change the initial density distribution to achieve better agreement with experiments. However, such approaches cannot be used to validate CFD codes as they rely on implicit confidence in the CFD code.

5.2 Jet in cross-flow

For the JICF problem, we also performed a study of the influence of the mesh size on the characteristic scales of the large-scale flow features similar to the one described in the beginning of section 5.1. In this case, the characteristic scales associated with the counter-rotating vortex pair dominating the flow are streamwise and spanwise penetration (Fig. 12).

Results for all three grids described in section 4.2 show similar trends. Transverse penetration is nearly grid independent by $x/D = 8$, while spanwise penetration is more sensitive to grid resolution. At $x/D = 9$, the difference between the medium and fine grid results is just 3%. The area enclosed by the 90% injected fluid concentration contour depends on the shape of the jet in the CRVP as well as the penetration quantities that indicate its outer dimensions. There is signifcant numerical diffusion on the coarse grid that is manifested in larger spanwise penetration and enclosed area. Thus it is clear that the coarse grid does not resolve the jet cross-section adequately. The medium grid was found to resolve the shock and vortical structures satisfactorily and was used for the remainder of the simulations. Grid convergence computations show that the order of convergence is just under 2, in agreement with more extensive grid convergence studies using GASP.

The flow features shown in Fig. 2 are adequately resolved in our simulations. These flow features are quite similar for the two injected fluids (air and helium). Figure 13 shows Mach number contours for air and helium injection, with which the upstream separation region, barrel shock, bow shock and Mach disk identified. Helium–injected flow has a stronger expansion in the barrel shock, reaching about Mach 7, while the flow with air injection reaches about Mach 6. For helium, the Mach disk is centered at $x/D \approx 1.8$, while for air it is centered at $x/D \approx 2.2$. Apart from these differences, the flow structure of the two cases is very similar.

In both cases, a horseshoe vortex system forms upstream of the jet, as shown by streamtrace visualization in Fig. 14. An (imaginary) cylinder of diameter D and length 1.2 D located at the origin is shown for reference. The horseshoe vortex system originates in the lower part of the upstream separated boundary layer. The crossflow is effectively blocked by the presence of the jet so that incoming fluid enters a recirculating region and then passes to one side of the jet. Upstream of the jet near the symmetry plane, the horseshoe vortex has negative z vorticity which is turned in the streamwise direction by the crossflow. While Fig. 14 shows the streamtraces for air injection, the horseshoe vortex for helium injection is very similar.

The wake vortex system[46] for the air injection case is shown by streamtraces in Fig. 15 along with the (imaginary) reference cylinder. The origin of the wake vortex is in another recirculating zone in the upper part of the upstream separated boundary layer. Upstream of the jet near the plane of symmetry, the wake vortex has positive z vorticity. The wake vortex wraps tightly around the jet to converge in its wake at $x/D \approx 3$, and then each leg diverges in the spanwise direction further downstream. Thus the spanwise vorticity is quickly converted to streamwise vorticity. It

should be noted that there is a single pair of wake vortices downstream of the jet. This is not obvious from the figure based on selected streamtraces. Although the wake vortex originates well above the horseshoe vortex, its legs approach the wall downstream of the jet, while the horseshoe vortex system remains at a nearly constant vertical height.

Results of the experiments and our predictions may be compared so long as it is noted that the experimental images indicate intensity of the Rayleigh/Mie scattering from particles in the crossflow (with black to white reversal). Gruber et al. [30, 35] hypothesize that the intensity is directly proportional to the concentration of particles in the mixed fluid, and is thus proportional to the mass fraction of crossflow fluid. With the black to white reversal, white in the images corresponds to mass fraction of jet fluid. No quantitative relationship between intensity of scattered light and particle concentration was reported. With this taken into consideration, our time-averaged predictions of crossflow mass fraction are compared with ensemble-averaged experimental images.

Figure 16 compares images from the experiments and our predictions of mass fraction of the crossflow fluid at several locations in the streamwise direction for both air and helium injections. Unlike the simulations, the experimental images do not resolve the fine structure associated with the jet cross-section in these end views of the y-z plane. Our results show good agreement with the experiments for the large-scale structure of the jet. The counter-rotating vortex pair (CRVP) becomes evident by $x/D = 4$. From our results, the case of helium injection has smaller regions of unmixed jet fluid as compared to air injection. At $x/D = 4$, helium injection also shows the significant effect of a secondary instability (with smaller scale) upon the primary CRVP instability. This is evident to a lesser extent for air. This secondary instability grows more rapidly downstream for helium injection, although the shape of the jet cross-section is similar between the two cases. Quantitative comparison between the penetration parameters in experiment and numerics (Fig. 17) shows a fairly good agreement, especially taking into consideration the rather limited nature of the experimental data.

6 Conclusion

We have performed two-dimensional numerical simulations of two validation problems involving shock acceleration of an initially diffuse heavy-gas (SF_6) cylinder embedded in lighter gas (air), and injection of a supersonic jet of gas (air or helium) into supersonic crossflow (air). Unlike many earlier simulations, this work uses a robust and hydrodynamically relatively simple code (*e.g.*, no adaptive mesh refinement) and limited computational resources, nevertheless producing overall good agreement with experiment.

The main conclusion of the validation exercises is that the hydrodynamic model of GASP is adequate for the numerical simulation of high-speed compressible mixing flows in chemical lasers. Two-dimensional simulations of intrinsically three-dimensional flow phenomena might be useful in predicting the macroscopic flow features, however, they cannot be expected to give a correct statistical prediction of the small scales important for mixing. In general, it is reasonalbe to expect the geometric parameters of large-scale flow features (counter-rotating vortex pairs) to be predicted with an error not exceeding 10-15%. The grid parameters and computational setup described here for the jet in crossflow should be adaptable to a specific chemical laser injector geometry.

References

[1] Palekar, A., Truman, C.R., and Vorobieff, P., 2005. Prediction of Transverse Injection of a Sonic Jet in Supersonic Crossflow. AIAA Paper AIAA-2005-5366, 36th AIAA Plasmadynamics and Lasers Conference, Toronto, Ontario, June 6-9, 2005.

[2] Palekar, A., Truman, C.R., and Vorobieff, P., 2004. Two-dimansional simulation of Richtmyer-Meshkov instability. B. Amer. Phys. Soc. 49(9), 201.

[3] Truman, C.R., Palekar, A., and Vorobieff, P. 2005. Predictions of transverse Injection of air or helium into supersonic crossflow. B. Amer. Phys. Soc. 50(9), 238.

[4] Palekar, A., Vorobieff, P., and Truman, C.R., 2005. Two-dimensional simulation of a shock-accelerated gas cylinder. Submitted to Prog. CFD, 2005.

[5] Hager, G. D., Watkins, L. J., Meyer, R. K., Johnson, D. E., Bean, L. J., and Loverro, D. L., 1987. A Supersonic Chemical Oxygen-Iodine Laser. Tech. Rep. TR-87-45, Air Force Weapons Laboratory.

[6] Buggeln, R. C., Shamroth, S., Lampson, A. I., and Crowell, P. G., 1994. Three-Dimensional (3-D) Navier-Stokes Analysis of the Mixing and Power Extraction in a Supersonic Chemical Oxygen Iodine Laser (COIL) with Transverse I_2 Injection. AIAA Paper 94-2435.

[7] Hishida, M., Azami, N., Iwamoto, K., Masuda, W., Fujii, H., Atsuta, T., and Muro, N., 1997. Flow and Optical Fields in a Supersonic Flow Chemical Oxygen Iodine Laser. AIAA Paper 97-2391.

[8] Madden, T. J., Hager, G. D., Lampson, A. I., and Crowell, P. G., 1999. An Investigation of Supersonic Mixing Mechanisms for the Chemical Oxygen-Iodine Laser (COIL). AIAA Paper 99-3429.

[9] Nikolaev, V. D., Zagidullin, M. V., Svistun, M. I., Anderson, B. T., Tate, R. F., and Hager, G. D., 2002. Results of Small-Signal Gain Measurements on a Supersonic Chemical Oxygen Iodine Laser with an Advanced Nozzle Bank. IEEE J. Quantum Electronics, **38**, 421–428.

[10] Zagidullin, M. V., Nikolaev, V. D., and Hager, G. D., 2004. High Gain, High Pressure, Highly Effcient COIL," Proc. SPIE, High-Power Laser Ablation V, **5448**, 1139–1149.

[11] Barmashenko, B., Rybalkin, V., Katz, A., and Rosenwalks, S., 2004. Parametric study of the Ben-Gurion University Efficient Supersonic Chemical Oxygen-Iodine Laser.Proc. SPIE, High-Power Laser Ablation V, **5448**, 282–293.

[12] Richtmyer, R.D., 1960. Taylor instability in shock-acceleration of compressible fluids. Commun. Pure and Appl. Math. **13**, 297–319.

[13] Meshkov, E. E, 1969. Instability of the interface of two gases accelerated by a shock wave. Sov. Fluid Dyn. **4 (5)**, 151–157.

[14] Arnett, W., Bahcall, J., Kirshner, R., and Woosley, S., 1989. Supernova 1987A. Annu. Rev. Astron. Astrophys. **27**, 629-700.

[15] Lindl, J.D., and Mead, W.C., 1975. Two dimensional simulation of fluid instability in laser fusion pellets. Phys. Rev. Lett. **34**, 1273–1276.

[16] Fishbine, J.M., 2002. Code validation experiments - a key to predictive Science. Los Alamos Research Quarterly.

[17] Marble, F.E., Hendricks, G.J, and Zukoski, E.E, 1987. Progress towards shock enhancement of supersonic combustion process. AIAA Paper 87-1880 .

[18] Yang, Y., Zhang, Q. and Sharp, D.H., 1994. Small amplitude theory of Richtmyer-Meshkov instability. Phys. Fluids **6 (5)**, 1856–1872.

[19] Vorobieff, P., Tomkins, C., Kumar, S., Goodenough, C., Mohamed, N.G. and Benjamin, R.F., 2004. Secondary instabilities in shock-induced transition to turbulence. Advances in Fluid Mechanics V, eds. Brebbia, Mendes and Rahman, WIT press, Southampton, UK/Boston, USA, 139.

[20] Peng, G., Zabusky, N.J., and Zhang, S., 2003. Vortex-accelerated secondary baroclinic vorticity deposition and late-intermediate time dynamics of a two-dimensional Richtmyer–Meshkov interface. Phys. Fluids, **15 (12)** 3730–3744.

[21] Zhang, S., Zabusky, N. J., Peng, G., and Gupta, S., 2004. Shock gaseous cylinder interactions: Dynamically validated initial conditions provide excellent agreement between experiments and numerical simulations to late-intermediate time. Phys. Fluids **16(5)**, 1203–1216.

[22] Velikovich, A.L. and Dimonte, G., 1996. Nonlinear perturbation theory of the incompressible Richtmyer-Meshkov instability. Phys. Rev. Lett. **76 (17)**, 3112–3115.

[23] Zhang, Q. and Sohn, SI., 1996. An analytical nonlinear theory of Richtmyer-Meshkov instability. Phys. Lett. A **212(3)**, 149–155.

[24] Rightley, P.M., Vorobieff, P. and Benjamin, R.F., 1997. Evolution of a shock-accelerated thin fluid layer. Phys. Fluids **9 (6)**, 1770–1782.

[25] Rightley, P. M., Vorobieff, P., Martin, R., Benjamin and R. F., 1999. Experimental observations of the mixing transition in a

shock-accelerated gas curtain. Phys. Fluids **11(1)**, 186–200.

[26] Budzinski, J.M. and Benjamin R.F., July 1994. Influence of initial conditions on the flow patterns of a shock-accelerated thin fluid layer. Phys. Fluids **6 (11)**, 3510–3512.

[27] Vorobieff, P., Mohamed, N. G., Tomkins, C., Goodenough, C., Marr-Lyon, M. and Benjamin, R. F., December 2003. Scaling evolution in shock-induced transition to turbulence. Phys. Rev. E **68**, 065301–065304.

[28] Tomkins, C., Prestridge, K., Rightley, P., Vorobieff, P. and Benjamin, R., 2002. Flow morphologies of two shock-accelerated gas cylinders. Journal of Visualization **5 (3)**, 273–283.

[29] Tomkins, C., Prestridge, K., Rightly, P., Marr-Lyon, M., Vorobieff, P. and Benjamin R., April 2003. A quantitative study of the interaction of two Richtmyer-Meshkov-unstable gas cylinders. Phys. Fluids **15 (4)**, 986–1004.

[30] Gruber, M. R., Nejad, A. S., Chen, T. H., and Dutton, J. C., 2000. Transverse Injection from Circular and Elliptical Nozzles into a Supersonic Crossflow. J. Propulsion and Power **16**, 449–457.

[31] Hermanson, J. C. and Winter, M., 1993. Mie scattering imaging of a transverse, sonic jet in supersonic flow. AIAA J. **31**, 129–132.

[32] Lee, M. P., McMillin, B. K., Palmer, J. K., and Hanson, R. K., 1992. Planar fluorescence imaging of a transverse jet in a supersonic crossflow. J. Propulsion and Power **8**, 729–735.

[33] VanLerberghe, W. M., Santiago, J. G., Dutton, J. C., and Lucht, R. P., 2000. Mixing of a sonic transverse jet injected into a supersonic flow. AIAA J. **28**, 470–479.

[34] Schetz, J. A., Thomas, R. H., and Billing, F. S., 1990. Mixing of transverse jets and wall jets in supersonic flow. Proc. IUTAM Symposium on Separated Flows and Jets, Novosibirsk, USSR, 1990, 807–837.

[35] Gruber, M. R., Nejad, A. S., and Dutton, J. C., 1996. An Experimental Investigation of Transverse Injection from Circular and Elliptical Nozzles into Supersonic Crossflow," Tech. Rep. WL-TR-96-2102, Wright-Patterson Air Force Base.

[36] Zoldi, C. A., 2002. A numerical and experimental study of a shock-accelerated heavy gas cylinder. PhD. Dissertation, Dept. of Applied Mathematics and Statistics, State University of New York, Stony Brook, NY.

[37] Aerosoft Inc., 2004. GASP version 4.2 user manual, Blacksburg, VA.

[38] Aerosoft, Company Background and History. Cited 24 March 2004.
      http://www.aerosft.com/Misc/aboutus.php

[39] Roe, P.L., 1981. Approximate Riemann solvers, parallel vectors, and difference schemes. J. Comput. Phys. **43**, 357–372.

[40] Viti, V., Schetz, J. A., and Neel, R., 2005. Comparison of First and Second Order Turbulence Models for a Jet/3D Ramp Combination in Supersonic Flow. AIAA Paper 2005-1100.

[41] Tannenhill, J. C., Anderson, D. A., and Pletcher, R. H., 1998. Computational Fluid Mechanics and Heat Transfer. Second Edition, Taylor & Francis, Philadelphia.

[42] Greenough, J.A., Rider, W.J., Zoldi, C., and Kamm, J.R. 2001. Code-to-code comparisons for the problem of shock acceleration of a diffuse dense gaseous cylinder. Proceedings of the 8th International Workshop on the Physics of Compressible Turbulent Mixing, Dec. 9-14 2001, Pasadena, CA.

[43] Rider, W.J., Greenough, J.A., and Kamm, J.R., 2003. Extrema, Accuracy and Monotonicity Preserving Methods for Compressible Flows, AIAA Paper 2003-4121, 16th AIAA CFD Conference, June 23-26, 2003, Orlando, Florida.

[44] Pointwise, Inc., Fort Worth, Texas, Gridgen Version 15 User Manual, 2004, ISBN 1-55395-989-2.

[45] Cebeci, T. and Bradshaw, P., Momentum Transfer in Boundary Layers, McGraw-Hill Book Company, 1977.

[46] Fric, T. R. and Roshko, A., 1994. Vortical structure in the wake of a transverse jet. J. Fluid Mech **279**, 147–159.

[47] Madden, T. J. and Miller, J. H., 2004. An analysis of mechanisms of flow unsteadiness in chemical oxygen-iodine laser flowfields. AIAA Paper 2004-2728.

[48] Howell, L.H., and Greenough, J.A., 2003. Radiation diffusion for multi-fluid Eulerian hydrodynamics with adaptive mesh refinement. J. Comp. Phys. **184 (1)**, 53–78.

[49] Dwarkadas, V. V., Plewa, T., Weirs, G., Tomkins, C., and Marr-Lyon, M. 2004. Simulation of vortex-dominated flows using the FLASH code. To appear in Proceedings of the Conference on Adaptive Mesh Refinement - Theory and Applications, Chicago, IL, September 3-5, 2003

[50] Vorobieff, P., Rivera, M.K., and Ecke, R.E., 1999. Soap film flows: Statistics of two-dimensional turbulence. Phys. Fluids **11 (8)**, 2167–2177.
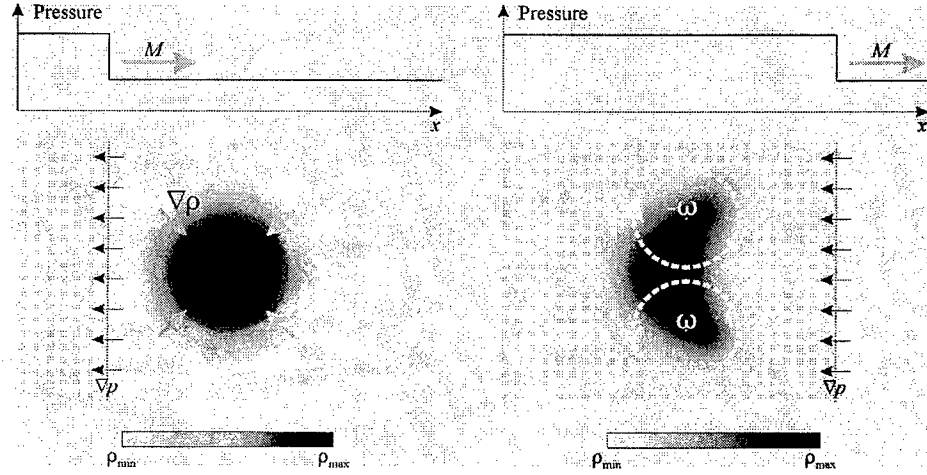
Figure 1: Schematic representation of a planar shock acceleration of an initially diffuse cylindrical density interface: left – prior to acceleration, right – after acceleration. Note the initial misalignment between gradients of pressure (black arrows) and density (gray arrows) leading to deposition of vorticity (white dashed arrows). Note that this schematic does not represent many of the subtle effects in the flow, *e.g.*, shock reflection or focusing.
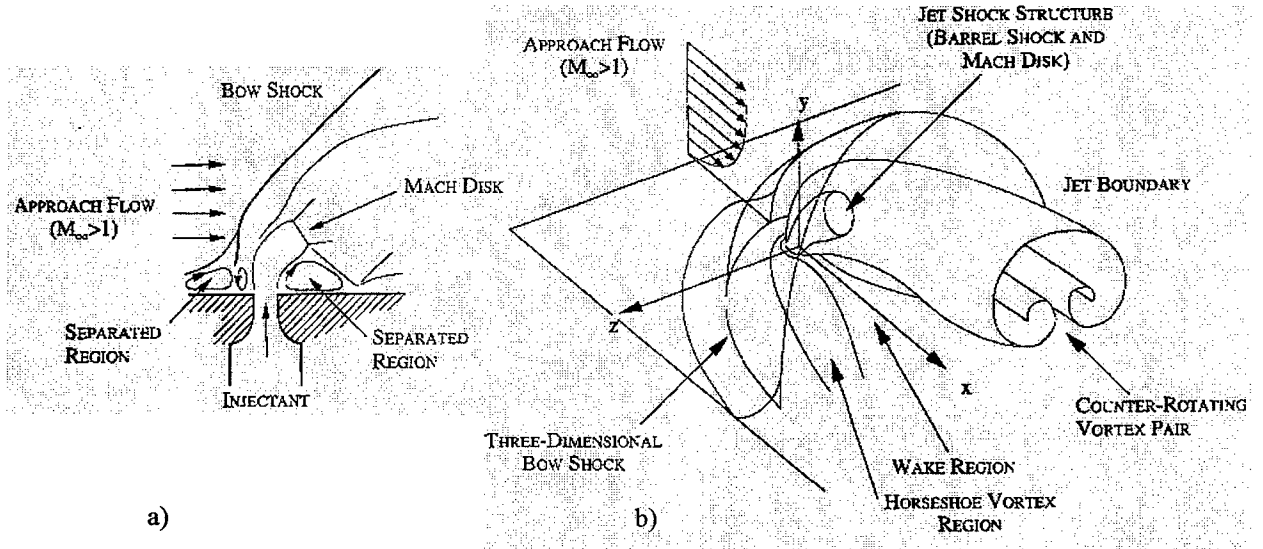
Figure 2: Schematic diagrams showing the vortical and shock structure of the JICF flow field (from Ref. [35]): (a) side view, (b) perspective view.
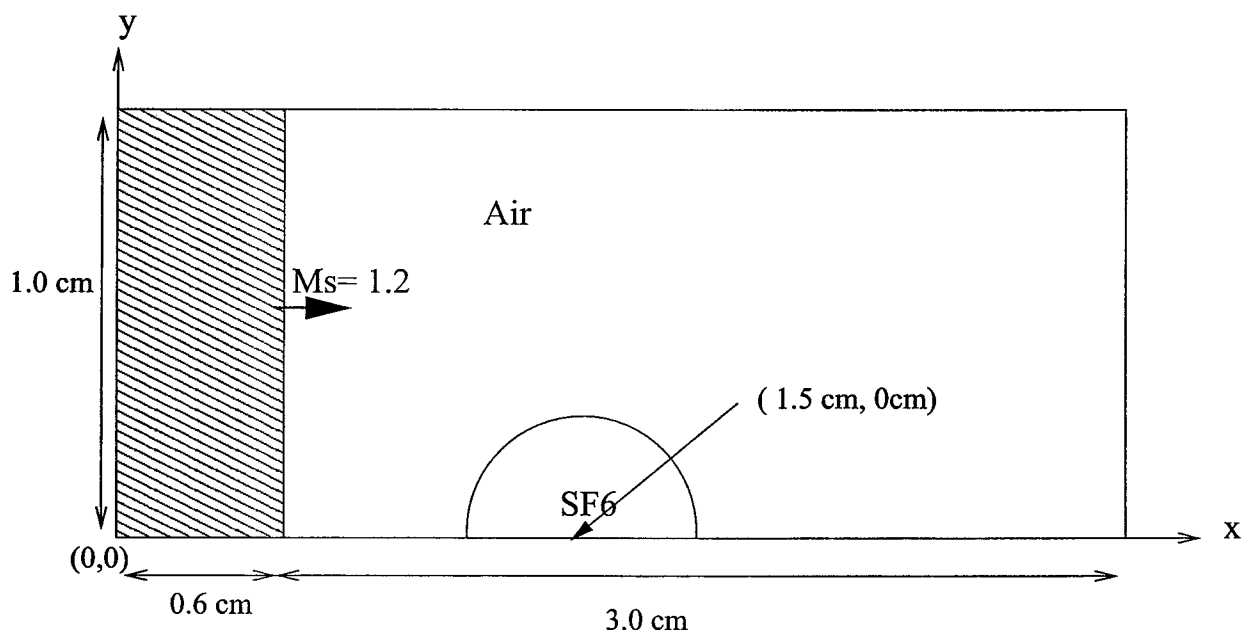
Figure 3: Computational domain for validation problem 1 (shock-accelerated gas cylinder). Note that only the top half of the actual domain is shown.

Along the length of the shock tube
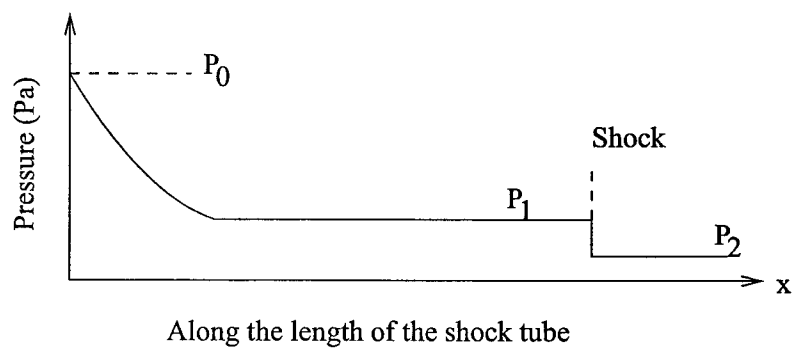
Figure 4: Pressure variation along the shock tube.
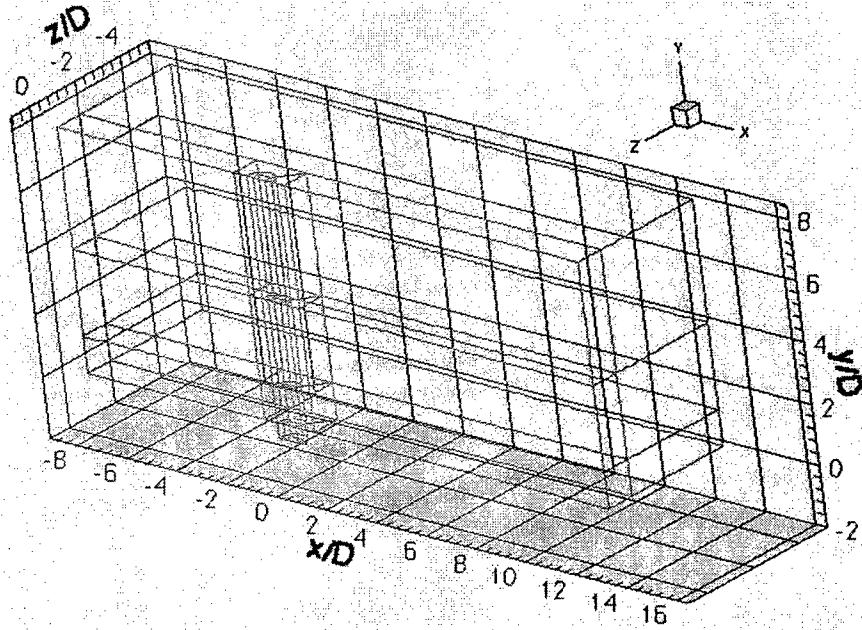
Figure 5: Schematic of the computational domain for validation problem 2 (jet in cross-flow) showing various grid zones.

Density field
(a)
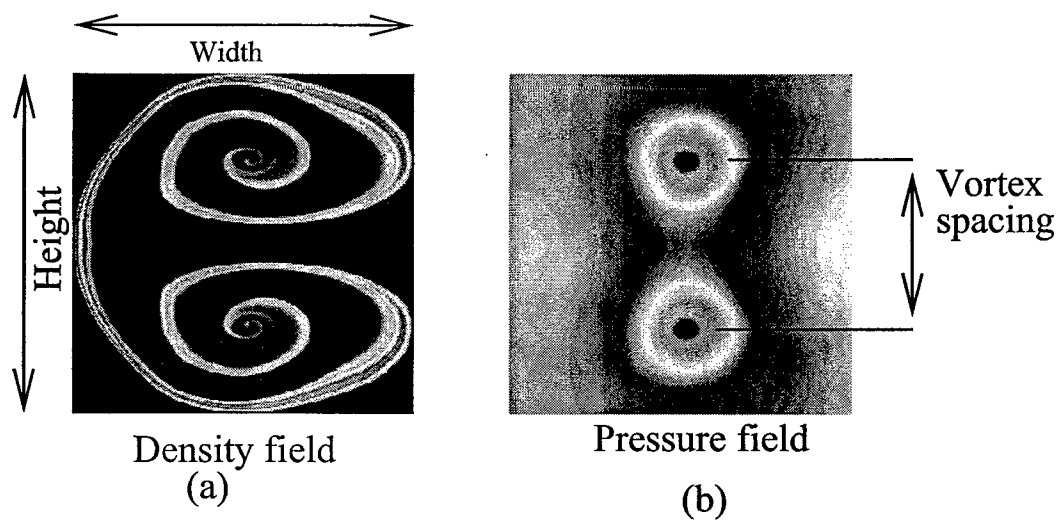
Pressure field
(b)

Figure 6: (a) The width and height of the mixing zone produced by shock-acceleration of the SF_6 cylinder. (b) Vortex spacing. Dark region corresponds to air in density field and low pressure in pressure field.
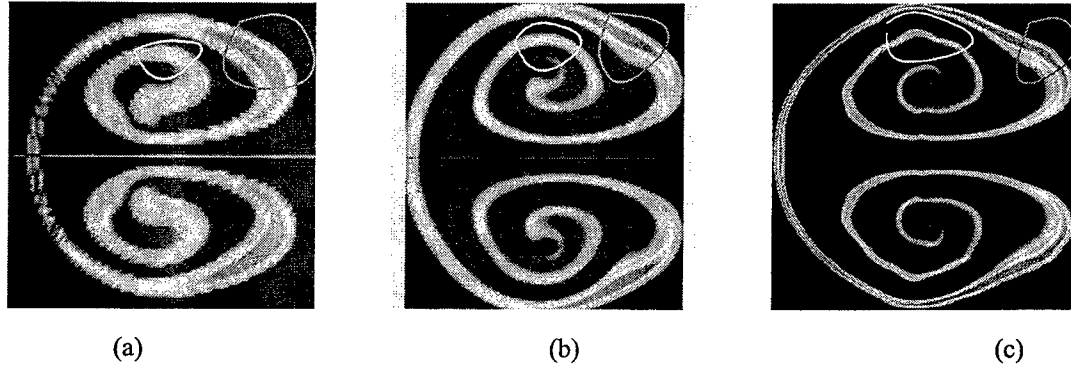
Figure 7: Effect of mesh spacing on the development of small scales in the shock-accelerated gas cylinder. (a) mesh spacing = 200 μm, (b) mesh spacing = 100 μm and (c) mesh spacing = 50 μm
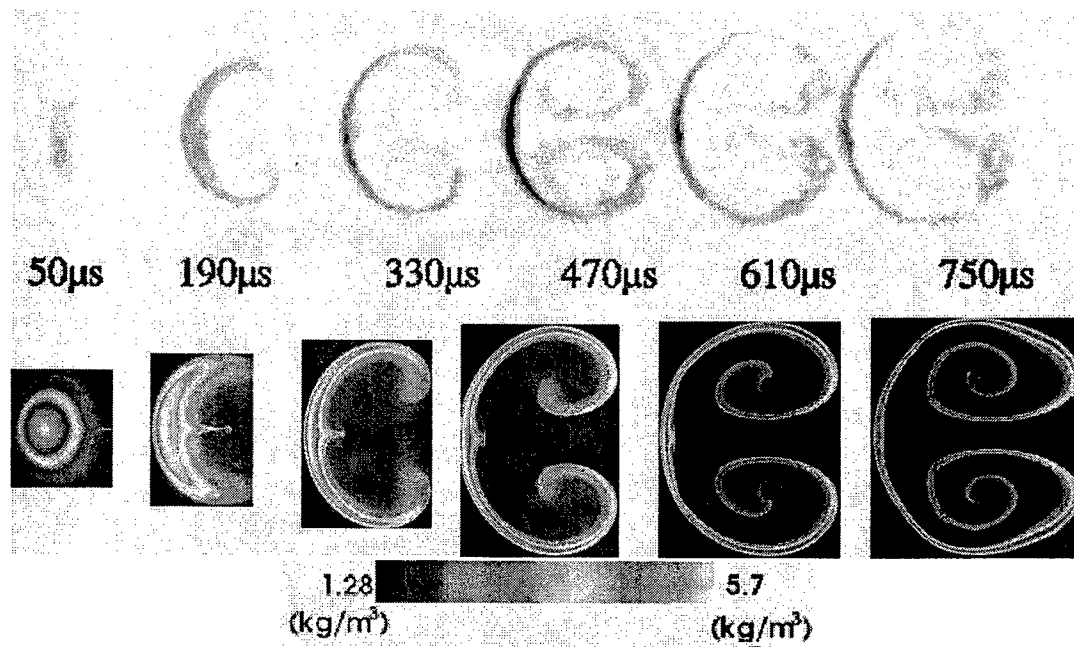
Figure 8: Comparison of experiment (top) and our numerical simulation (bottom). In experimental images dark color corresponds to higher SF_6 concentration. In numerics blue color corresponds to air.
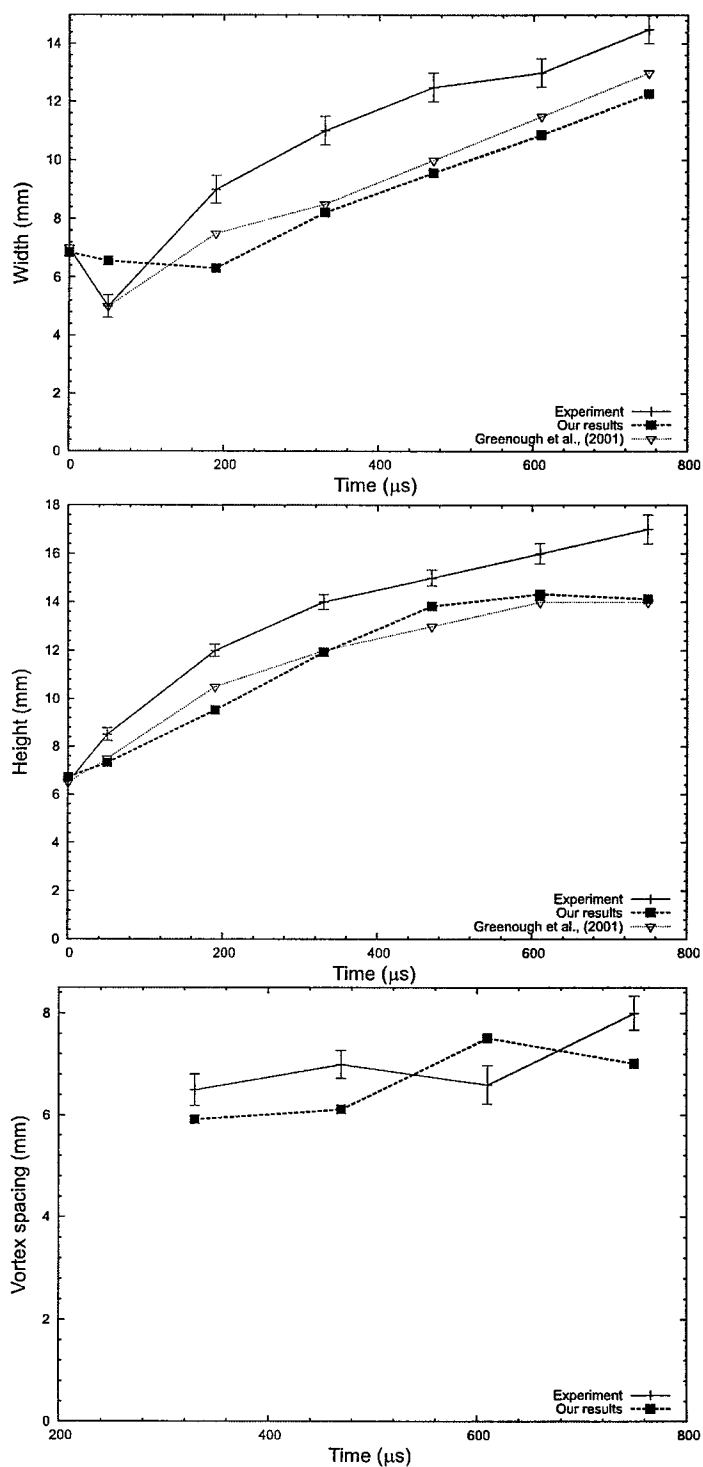
Figure 9: Comparison of mixing zone height (top), width (middle) and vortex spacing (bottom) between experiment and simulation.
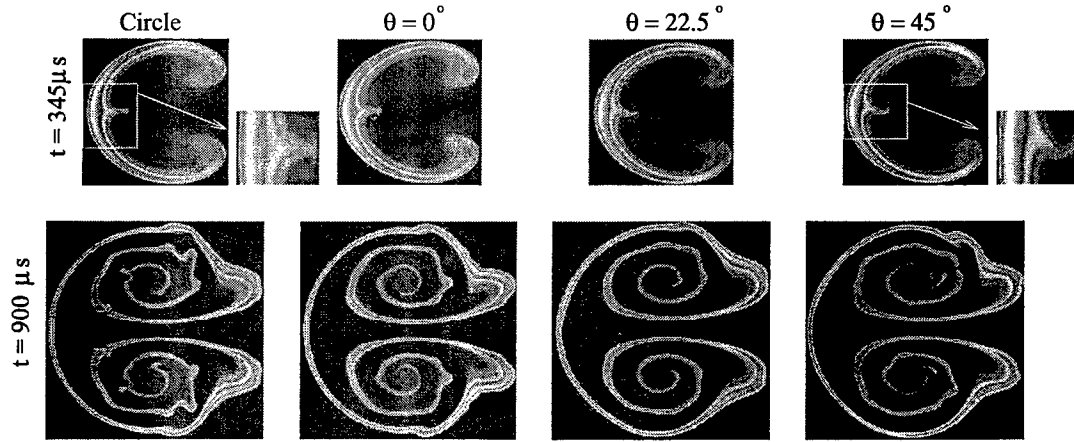
Figure 10: Flow morphology for different initial conditions. Top : at time = 345 μs and bottom : at time = 900 μs. The first image in both rows corresponds to the circular distributions while all other images are for elliptical conditions. Closeup shows the notch.
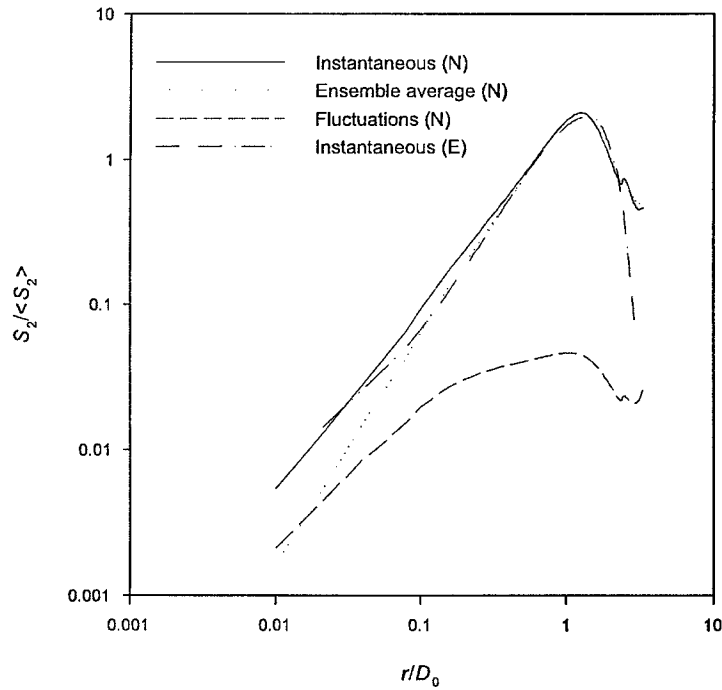
Figure 11: Second-order longitudinal velocity structure functions of instantaneous, ensemble-averaged and fluctuating velocity fields obtained from elliptic ICs (see text) at $\sim$ 900 μs. The structure functions are normalized by their average value, the scale r is normalized by the nominal gas cylinder diameter D_0. The second-order velocity structure function obtained in experiment [27] at $\sim$ 760 μs is shown for comparison. Experimental and numerical data are labeled 'E' and 'N' respectively in the captions.
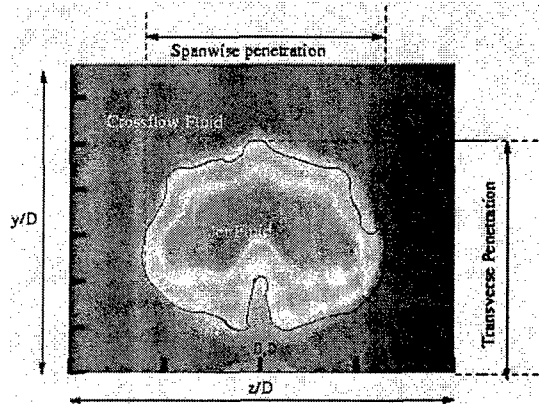
Figure 12: Schematic of an arbitrary end view (at fixed downstream location x/D) showing crossflow fluid mass fraction contours and transverse and spanwise penetration scales. Red denotes pure jet fluid and blue denotes pure crossflow fluid. D is the diameter of the injector.

Mach Number: 0.5 1.9 3.3 4.7 6.1 7.5
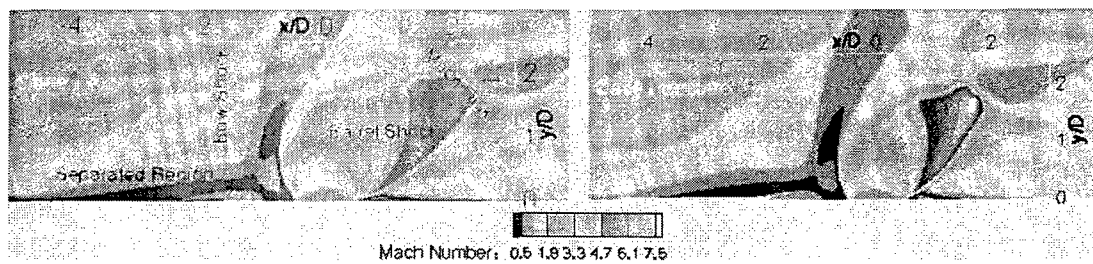
Figure 13: Jet in crossflow: Mach number contours in the $x - y$ plane at the centerline ($z = 0$, or plane of symmetry) for two injected fluids (air, left, and helium, right). Shock structures and upstream recirculating region are identified.
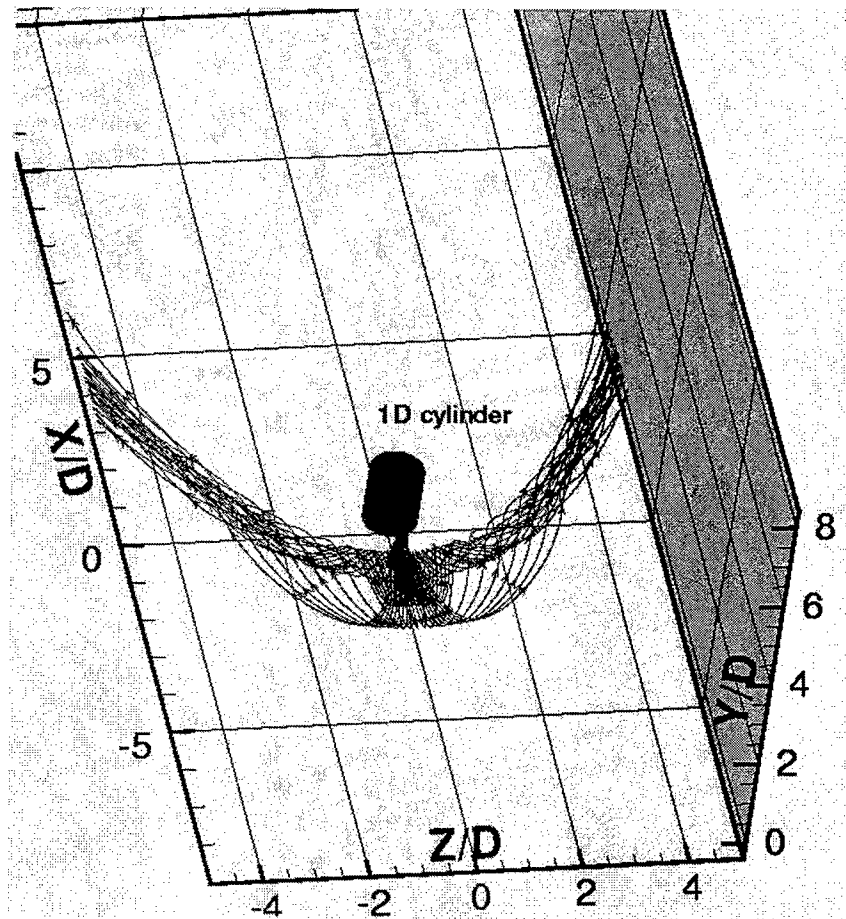
Figure 14: Jet in crossflow (air injection): streamtraces showing the horseshoe vortex system, along with an (imaginary) cylinder of diameter D and length $1.2\,D$ located at the origin shown for reference.
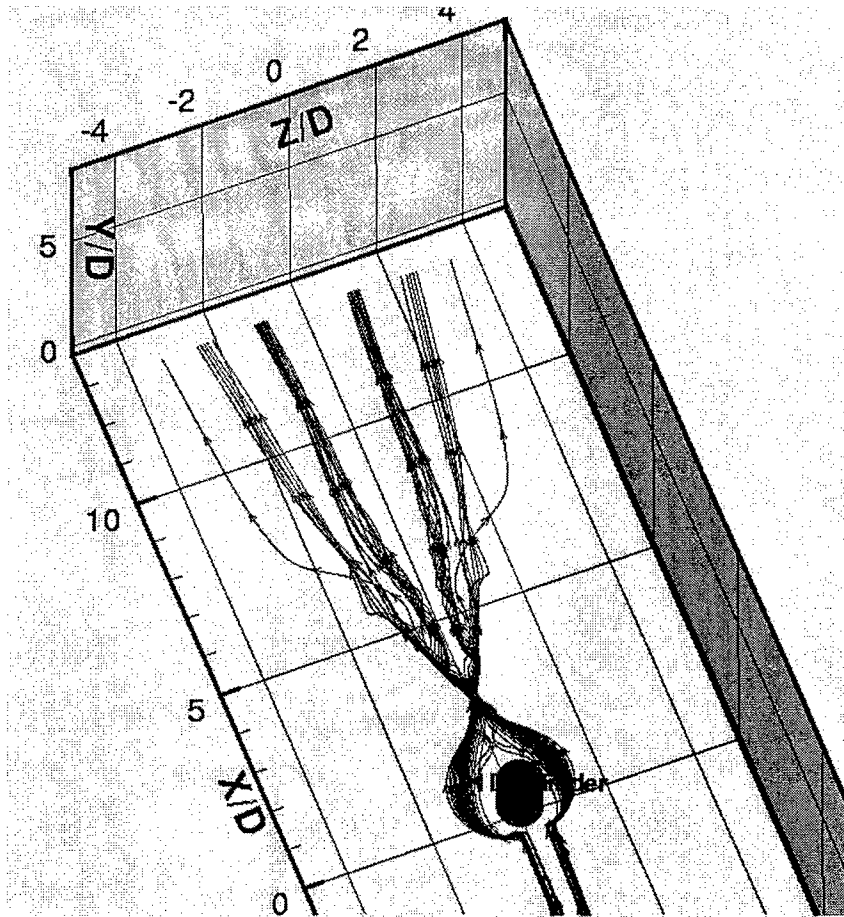
Figure 15: Jet in crossflow (air injection): streamtraces illustrating the wake vortex system, along with an (imaginary) cylinder of diameter D and length $1.2\ D$ located at the origin shown for reference.
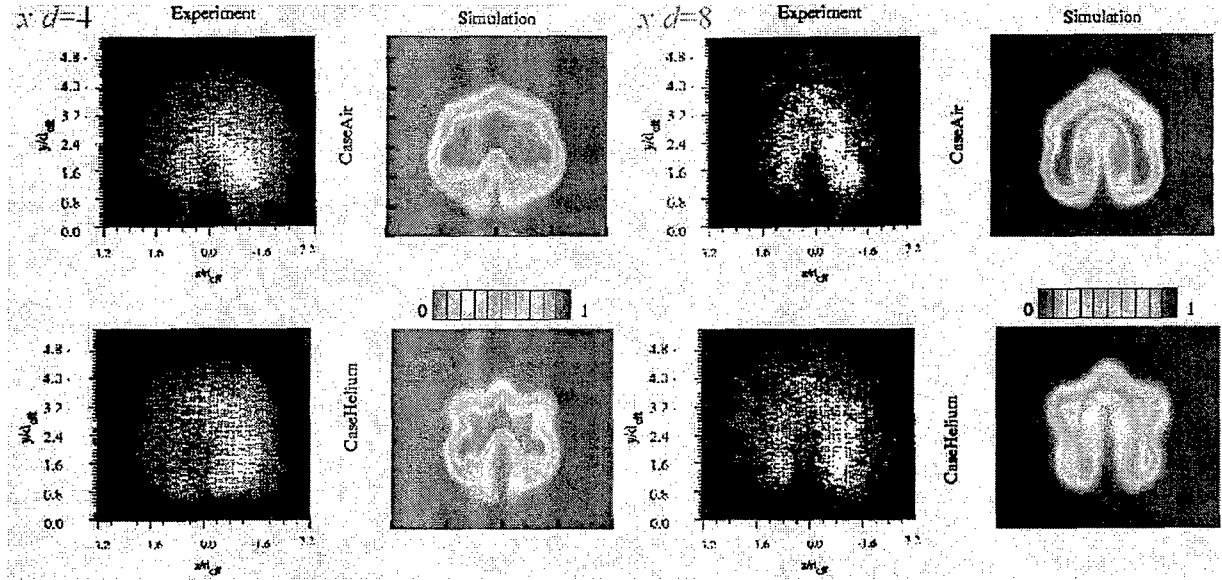
Figure 16: Mass fraction of the crossflow fluid for end views ($y - z$ plane) at downstream distances $x/D = 4$ (left) and $x/D = 8$ (right). The left column shows experimental measurements of Gruber et al.[30, 35] with our predictions in the right column. Black corresponds to 100% crossflow fluid, while white corresponds to 0% crossflow fluid (or 100% jet fluid). For each downstream position, results for air injection are shown on top and results for helium injection are shown on the bottom.
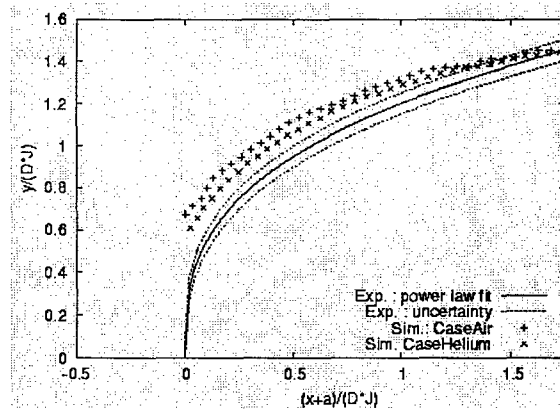

Figure 17: Jet in crossflow penetration based on a side view of the $x - y$ plane at $z = 0$. Here the jet-to-crossflow momentum ratio is $J = 2.90$ and $a = D/2$.

REPORT DOCUMENTATION PAGE

1. REPORT DATE (DD-MM-YYYY)	2. REPORT TYPE		3. DATES COVERED (From - To)
17-04-2006	Final		Nov 2004 - Nov 2005

4. TITLE AND SUBTITLE	5a. CONTRACT NUMBER
Prediction of Chemical Laser Flow	
	5b. GRANT NUMBER
	FA9550-05-1-0031
	5c. PROGRAM ELEMENT NUMBER

6. AUTHOR(S)	5d. PROJECT NUMBER
Truman, C. Randall	
Vorobieff, Peter	5e. TASK NUMBER
	5f. WORK UNIT NUMBER

7. PERFORMING ORGANIZATION NAME(S) AND ADDRESS(ES)	8. PERFORMING ORGANIZATION REPORT NUMBER
Mechanical Engineering Department University of New Mexico Albuquerque NM 87131	n/a

9. SPONSORING/MONITORING AGENCY NAME(S) AND ADDRESS(ES)	10. SPONSOR/MONITOR'S ACRONYM(S)
Air Force Office of Scientific Research 4015 Wilson Blvd, Room 713 Arlington VA 22203-1954 Dr. Michael Berman	AFOSR
	11. SPONSOR/MONITOR'S REPORT NUMBER(S)
	n/a

12. DISTRIBUTION/AVAILABILITY STATEMENT	
Approve for Public Release: Distribution Unlimited	AFRL-SR-AR-TR-06-0130

13. SUPPLEMENTARY NOTES

14. ABSTRACT
Numerical simulations of high-speed mixing flows were carried out using GASP, a computational fluid dynamics (CFD) code. The ultimate goal is to use GASP for prediction and optimization of chemical laser flows. Numerical simulations were used for code validation. Two validation exercises, for which experimental data was available for comparison, include:
1) Simulation of shock-accelerated mixing flow subject to Richtmyer-Meshkov instability, and
2) Jet-in-Crossflow problem for a supersonic jet discharging into a supersonic crossflow.
The agreement with experimental data was quite good. Subtle features of the flow not apparent in the measurements were revealed by the simulations. The numerical scheme and turbulence model in GASP were found to be quite good for mixing flows typical of chemical laser nozzles with injection.

15. SUBJECT TERMS
chemical lasers, code validation, compressible flow, turbulent mixing

16. SECURITY CLASSIFICATION OF:			17. LIMITATION OF ABSTRACT	18. NUMBER OF PAGES	19a. NAME OF RESPONSIBLE PERSON
a. REPORT	b. ABSTRACT	c. THIS PAGE			C. Randall Truman
U	U	U	UU	24	19b. TELEPHONE NUMBER (Include area code) (505)277-6296